Core Structure of S2 from the Human Coronavirus NL63 Spike Glycoprotein[†,‡]

Qi Zheng,[§] Yiqun Deng,[§] Jie Liu,[§] Lia van der Hoek,[||] Ben Berkhout,[||] and Min Lu*[,§]

Department of Biochemistry, Weill Medical College of Cornell University, New York, New York 10021, and Department of Human Retrovirology, Academic Medical Center, University of Amsterdam, Amsterdam, The Netherlands

Received August 18, 2006; Revised Manuscript Received October 17, 2006

ABSTRACT: Human coronavirus NL63 (HCoV-NL63) has recently been identified as a causative agent of acute respiratory tract illnesses in infants and young children. The HCoV-NL63 spike (S) protein mediates virion attachment to cells and subsequent fusion of the viral and cellular membranes. This viral entry process is a primary target for vaccine and drug development. HCoV-NL63 S is expressed as a single-chain glycoprotein and consists of an N-terminal receptor-binding domain (S1) and a C-terminal transmembrane fusion domain (S2). The latter contains two highly conserved heptad-repeat (HR) sequences that are each extended by 14 amino acids relative to those of the SARS coronavirus or the prototypic murine coronavirus, mouse hepatitis virus. Limited proteolysis studies of the HCoV-NL63 S2 fusion core identify an α-helical domain composed of a trimer of the HR segments N57 and C42. The crystal structure of this complex reveals three C42 helices entwined in an oblique and antiparallel manner around a central triple-stranded coiled coil formed by three N57 helices. The overall geometry comprises distinctive high-affinity conformations of interacting cross-sectional layers of the six helices. As a result, this structure is unusually stable, with an apparent melting temperature of 78 °C in the presence of the denaturant guanidine hydrochloride at 5 M concentration. The extended HR regions may therefore be required to prime the group 1 S glycoproteins for their fusion-activating conformational changes during viral entry. Our results provide an initial basis for understanding an intriguing interplay between the presence or absence of proteolytic maturation among the coronavirus groups and the membrane fusion activity of their S glycoproteins. This study also suggests a potential strategy for the development of improved HCoV-NL63 fusion inhibitors.

The coronavirus family of enveloped positive-stranded RNA viruses includes significant human and animal pathogens. The newly identified SARS[1] coronavirus (SARS-CoV) was found to be the etiological agent of the 2002−2003 epidemic of severe acute respiratory syndrome (SARS) that killed nearly 10% of infected individuals (*1*, *2*). Human coronavirus 229E (HCoV-229E) and human coronavirus OC43 (HCoV-OC43) are endemic and responsible for up to 30% of mild upper respiratory tract infections (*3*, *4*). The human coronavirus NL63 (HCoV-NL63) has recently been associated with conjunctivitis, croup, and acute respiratory infections in children and immunocompromised patients (*5*−*8*). On the basis of genetic and serological relationships (*3*, *9*), HCoV-NL63 is closely related to the group 1 coronaviruses that include HCoV-229E and animal coronaviruses like porcine epidemic diarrhea virus, transmissible gastroenteritis virus, and feline infectious peritonitis virus, whereas HCoV-OC43 is a group 2 virus, related to animal coronaviruses like mouse hepatitis virus (MHV), porcine hemagglutinining encephalomyelitis virus, and bovine coronavirus. SARS-CoV and SARS-CoV-like viruses found in animals are outliers of group 2 and have been assigned to group 4 (*10*−*12*). The factors that influence the evolution and pathogenicity of coronaviruses remain largely unknown. Recent work suggests that the species tropism and virulence of a specific coronavirus are largely determined by its spike (S) glycoprotein (*13*−*19*). The S proteins mediate virion attachment to cells and subsequent fusion of the virus and cell membranes and are the major antigenic determinants of coronaviruses (*20*, *21*).

Coronavirus S proteins are synthesized as single polypeptide chains that oligomerize in the endoplasmic reticulum and are processed through the Golgi, eventually forming long, petal-shaped spikes that protrude from the virion surface (*20*). By analogy with a large group of so-called class I fusion proteins, coronavirus S proteins consist of an N-terminal receptor-binding domain (S1) and a C-terminal transmembrane fusion domain (S2) (*21*−*23*). In some cases such as MHV and HCoV-OC43, the glycoprotein precursor requires proteolytic cleavage to generate the mature S1 and S2 chains by a furin-like protease in the producer cell (*22*, *24*−*27*). By contrast, the S proteins of SARS-CoV, HCoV-

[†] This work was supported by National Institutes of Health Grant AI042382 and by the Irma T. Hirschl Trust.

[‡] The atomic coordinates and structure factors have been deposited in the RCSB Protein Data Bank (2IEQ).

* Corresponding author. Phone: (212) 746-6562. Fax: (212) 746-8875. E-mail: mlu@med.cornell.edu.

[§] Weill Medical College of Cornell University.

[||] University of Amsterdam.

[1] Abbreviations: HCoV, human coronavirus; S, spike protein; HR, heptad repeat; CoV, coronavirus; SARS, severe acute respiratory syndrome; MHV, mouse hepatitis virus; ACE2, angiotensin-converting enzyme 2; CD13, aminopeptidase N; HIV, human immunodeficiency virus; HPLC, high-performance liquid chromatography; CD, circular dichroism; TBS, Tris-buffered saline; GuHCl, guanidine hydrochloride; $[\theta]_{222}$, molar ellipticity at 222 nm; T_m, midpoint of the thermal unfolding transition; rms, root-mean-square.

10.1021/bi061686w CCC: $33.50
Published on Web 12/01/2006

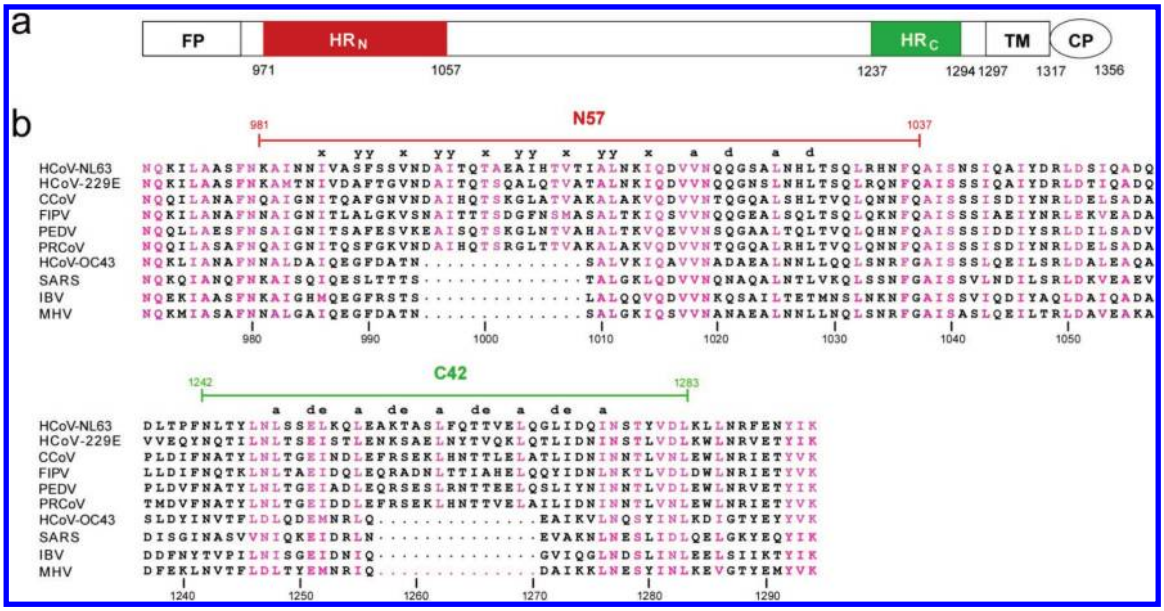

FIGURE 1: Interactions of two heptad-repeat regions in HCoV-NL63 S2. (a) Schematic representation of S2. The positions of the fusion peptide (FP), the two hydrophobic heptad repeats (HR_N and HR_C), the transmembrane region (TM), and the cytoplasmic region (CP) are shown. (Note that the exact location of the fusion peptide is not known.) Residues are numbered according to their position in the HCoV-NL63 S sequence. (b) Sequence alignment of the HR_N (top) and HR_C (bottom) regions derived from coronavirus S2 proteins. The sequences are shown for HCoV-NL63 (AAS58177), HCoV-229E (AAK32191), CCoV (canine coronavirus; AAQ17220), FIPV (feline infectious peritonitis virus; BAA06805), PEDV (porcine epidemic diarrhea virus; AAT75298), PRCoV (porcine respiratory coronavirus; CAA42686), HCoV-OC43 (S44241), SARS-CoV (AAP13441), IBV (avian infectious bronchitis virus; AAO34396), and MHV (mouse hepatitis virus; P11225). The locations of the N57 and C42 peptides from HCoV-NL63 S2 are indicated. Buried core residue positions of the N57/C42 complex are shown (see text and Figures 4 and 5). Chemically similar residues among coronaviruses are colored red.

229E, and HCoV-NL63 lack furin recognition sites and are found uncleaved on the virion surface (*28*−*30*). Host-cell receptors for several human coronaviruses have been identified. For example, SARS-CoV and HCoV-NL63 employ angiotensin-converting enzyme 2 (ACE2) as a receptor (*31*, *32*), and HCoV-229E engages aminopeptidase N (CD13) (*33*, *34*). Following receptor binding, coronaviruses are endocytosed and enter cells by pH-dependent fusion in the endosome (*31*, *35*−*37*). In addition, coronavirus S proteins can mediate cell−cell fusion at neutral pH (*24*, *25*, *32*, *35*, *38*, *39*). Although the activation triggers appear to differ in virus−cell and cell−cell fusion, in both cases the S2 domain undergoes large-scale conformational changes in order to bring two membranes into close apposition and induce fusion, a process that results in the release of the virion core into the cell cytoplasm (*40*−*44*).

Coronavirus S2 proteins share several characteristic features with other known class I fusion proteins, including influenza virus HA_2 and HIV-1 gp41. A hydrophobic fusion peptide, which is exposed and inserted into the target-cell membrane during the fusion process (*41*), is presumably located at the N-terminal region of S2 (Figure 1a). S2 is a type I integral membrane protein with a single transmembrane domain. Flanking both the fusion peptide and transmembrane domains are two highly conserved regions consisting of heptad repeats (HR) of hydrophobic residues characteristic of coiled coils. These regions are denoted HR_N and HR_C, respectively, and are separated by ~250 intervening amino acids. Structural studies of soluble S2 cores from SARS-CoV and MHV showed that the HR_N and HR_C segments associate to form a highly stable six-helix bundle (*22*, *45*−*52*). Three HR_C helices pack in the antiparallel manner into three hydrophobic grooves on the surface of an interior trimeric coiled coil formed by three HR_N helices. This six-helix bundle is a well-known structural motif of class I fusion proteins and may in fact be the final fusogenic form of S2 (*40*−*43*). Current thinking postulates that formation of the six-helix bundle is mechanistically and thermodynamically linked to merging of the viral and cellular membranes (*52*−*54*).

Peptides corresponding to the HR_C region of S2 can inhibit SARS-CoV and HCoV-NL63 infection at micromolar concentrations (*50*, *55*, *56*). Analogous to the HIV-1 gp41 peptide fusion inhibitors (*40*), these S2 HR_C peptides have been proposed to act in a dominant−negative manner to interfere with six-helix bundle formation, thereby inhibiting coronaviral entry. Interestingly, there are 14-residue in-phase insertions in both HR sequences of all known group 1 coronaviruses including HCoV-229E and HCoV-NL63 (Figure 1b). It remains unclear how these sequence elements affect the folding to, or stability of, the fusogenic conformation of S2. A detailed mechanistic understanding of interactions between the HR regions in a group 1 virus should help clarify the mechanism of membrane fusion mediated by the S protein and could assist antiviral drug and vaccine development. Here we have used a protein-dissection approach to identify and determine the X-ray crystal structure of a proteolytically resistant S2 core from HCoV-NL63, and we discuss the implications of this structure for coronaviral membrane fusion and its inhibition.

MATERIALS AND METHODS

Protein Expression, Purification, and Proteolysis. The HCoV-NL63 S2 HR_N/HR_C segments (representing residues 981−1046 and 1237−1286 of full-length S; Figure 1a) were cloned into the pET24a vector (Novagen) to generate pN66/C50 using standard molecular biology techniques. Plasmid

pN66(L6)C50 was derived from pN66/C50 by the insertion of a Ser-Gly-Gly-Arg-Gly-Gly sequence between the C terminus of the N66 segment and the N terminus of the C50 segment. The N57(L10)C42 protein consists of residues 981−1037 and 1242−1283 connected by the linker residues Ser-Gly-Gly-Arg-Gly-Ser-Gly-Arg-Gly-Gly. All constructs were appended to the TrpLE′ leader sequence (*57*). The N66-(L6)C50 and N57(L10)C42 proteins were expressed in *Escherichia coli* BL21 (DE3)/pLysS, purified from inclusion bodies, and cleaved from the TrpLE′ leader sequence with cyanogen bromide as described (*58*). All peptide proteins were purified to homogeneity by reverse-phase HPLC (Waters, Inc.) on a Vydac C18 preparative column (Hesperia, CA) using a water−acetonitrile gradient in the presence of 0.1% trifluoroacetic acid and lyophilized. Protein identities were confirmed by electrospray mass spectrometry (PerSeptive Biosystems Voyager Elite, Cambridge, MA). Proteinase K digestion was performed at protease/protein ratios of 1:200 (wt/wt) and room temperature in 50 mM Tris−HCl (pH 8.0). Proteolytic fragments were analyzed by reverse-phase HPLC and assigned by N-terminal sequencing and mass spectrometry. Protein concentrations were determined by using the method of Edelhoch (*59*).

Circular Dichroism Spectroscopy. CD experiments were performed on an Aviv 62A/DS (Aviv Associates, Lakewood, NJ) spectropolarimeter equipped with a thermoelectric temperature control in TBS (50 mM Tris−HCl, pH 8.0, 150 mM NaCl) and 50 μM protein. CD spectra were collected from 260 to 200 nm at 4 °C, using an average time of 5 s, a cell path length of 0.1 cm, and a bandwidth of 1 nm. A $[\theta]_{222}$ value of −35 000 deg cm^2 dmol^{-1} was taken to correspond to 100% helix (*60*). Thermal stability was determined by monitoring $[\theta]_{222}$ as a function of temperature in TBS (pH 8.0) and with the addition of 5 M guanidine hydrochloride (GuHCl) to facilitate unfolding. Thermal melts were performed in 2° intervals with a 2 min equilibration at the desired temperature and an integration time of 30 s. Reversibility was verified by repeated scans. Superimposable folding and unfolding curves were observed, and >95% of the signal was regained upon cooling. Values of midpoint unfolding transitions (T_m) were estimated by evaluating the maximum of the first derivative of $[\theta]_{222}$ versus temperature data (*61*).

Sedimentation Equilibrium Analysis. Analytical ultracentrifugation measurements were carried out on a Beckman XL-A (Beckman Coulter) analytical ultracentrifuge equipped with an An-60 Ti rotor (Beckman Coulter) at 20 °C. Protein samples were dialyzed overnight against TBS (pH 8.0), loaded at initial concentrations of 25, 100, and 400 μM, and analyzed at rotor speeds of 10, 16, and 19 krpm. Data were acquired at two wavelengths per rotor speed setting and processed simultaneously with a nonlinear least-squares fitting routine (*62*). Solvent density and protein partial specific volume were calculated according to solvent and protein composition, respectively (*63*). Nonrandom residuals, indicative of aggregation or derivation from ideality, were observed for N66(L6)C50. The apparent molecular mass of N57(L10)C42 was within 10% of that calculated for an ideal trimer, with no systematic deviation of the residuals.

Crystallization and Data Collection. HPLC-purified N57-(L10)C42 was solubilized in 6 M GuHCl and 50 mM Tris−HCl (pH 8.0) and refolded by dilution into TBS (pH 8.0).

Table 1: Summary of Crystallographic Analysis

Data Collection	
resolution (Å)	51.6−1.75
unique reflections	25668
redundancy	3.2 (3.1)[a]
completeness (%)	95.6 (98.1)
R_{merge} (%)[b]	6.8 (36.3)
$I/\sigma(I)$	10.7 (3.7)
space group	$P2_1$
unit cell parameter	$a = 50.0$ Å, $b = 51.7$ Å, $c = 54.1$ Å, $\beta = 107.6°$
molecules in AU	3
solvent content (%)	32.2
Refinement	
resolution (Å)	51.6−1.75
reflections	24376
R_{cryst} (%)[c]	19.6
R_{free} (%)[c]	24.0
protein atoms	2009
water molecules	228
sodium ions	3
acetic ion	1
rms Deviations from Ideal Geometry	
bond lengths (Å)	0.02
bond angles (deg)	1.5
torsion angles (deg)	4.5
B-values (Å^2)	2.6

[a] Values in parentheses refer to the highest-resolution shell 1.75−1.81 Å. [b] $R_{merge} = \Sigma|I - \langle I\rangle|/\Sigma I$, where I is the integrated intensity of a given reflection. [c] $R_{cryst} = \Sigma|F_o - F_c|/\Sigma F_o$. $R_{free} = R_{cryst}$ calculated using 5% of the reflection data chosen randomly and omitted from the start of refinement.

The protein was repurified by size exclusion on a Superdex 200 column equilibrated with TBS (pH 8.0), exchanged into 10 mM Tris−HCl (pH 8.0), and concentrated to 20 mg/mL by ultrafiltration. N57(L10)C42 was crystallized using the hanging drop vapor diffusion method by equilibrating against reservoir buffer (0.7 M sodium acetate, 0.2 M imidazole buffer, pH 5.15), a solution containing 1 μL of 6 mg/mL protein and 1 μL of reservoir buffer. Crystals belong to space group $P2_1$ ($a = 50.0$ Å, $b = 51.7$ Å, $c = 54.1$ Å, $\beta = 107.6°$) and contain three monomers in the asymmetric unit, with a solvent content of 32.2% (Table 1). The crystals were harvested in 0.6 M sodium acetate, 0.2 M imidazole buffer, pH 5.15, 25% PEG 400 and frozen in liquid nitrogen. Diffraction data were recorded at 100 K on a MAR345 image plate at the beamline X4C of the National Synchrotron Light Source at Brookhaven National Laboratory. The images were indexed and integrated using a monoclinic unit cell with the program DENZO (*64*). The intensities were scaled in *P*2 symmetry wih the program SCALEPACK (*64*); the systematic absence of intensities indicates a 2-fold screw axis.

Structure Determination. Initial phases were determined by molecular replacement with the program Phaser (*65*) using the structure of the SARS-CoV N50/C36 trimer (1ZV8) as a search model. Three N56/C36 molecules were oriented and placed in the asymmetric unit with a *Z* score of 7.6 and a final refined LLG of 227. In order to remove model bias, this model and the dataset for N57(L10)C42 were directly fed to the program Arp/Warp (*66*), which allowed ∼71% of the final model to be automatically traced. The resulting experimental electron density map was of excellent quality and showed the location of most of the side chains. Although some electron density was evident for the linker loop region, no model could be built into it. Density interpretation and

manual model building were done with the program O (*67*). Crystallographic refinement of the model was carried out by using Refmac (*68*), resulting in the R_{free} of 29.0% and the R_{work} of 24.5% between 51.6 and 1.75 Å resolution. At this stage, three sodium ions (near the N termini of the C42 helices), one acetate ion, and water molecules were modeled in the electron density. The three tentatively assigned metal atoms are 8.6, 6.5, and 4.4 σ electron density peaks (in difference maps calculated with phases from the refined model) and refined to *B*-factors of 22.8, 22.4, and 28.8 Å^2, respectively. These peaks are hexahedrally coordinated in the crystal by the five oxygen or nitrogen atoms of the protein and one water molecule, characteristic of metal ions. Refinement was concluded using Refmac (*68*) with TLS groups assigned for each N57 or C42 monomer (*69*). The final model (R_{cryst} = 19.6% and R_{free} = 24.0% for the resolution range 51.6−1.75 Å) consists of residues 982−1031 and 1243−1280 (monomer A), 981−1032 and 1243−1279 (monomer B), and 981−1032 and 1244−1279 (monomer C) in the asymmetric unit, three sodium ions, one acetate ion, and 228 water molecules. Bond lengths and bond angles of the model have root-mean-square (rms) deviations from ideality of 0.02 Å and 1.5°, respectively. All protein residues are in the most favored regions of the Ramachandran plot.

Structure Analysis. Coiled-coil parameters were calculated by fitting the C_α backbones to a supercoil parametrization suggested by Crick (*70*). The local pitch values as a function of residue number were obtained with TWISTER (*71*). The rms deviations were calculated with LSQKAB in the CCP4i program suite (*72*). Buried surface areas were calculated from the difference of the accessible side-chain surface areas of the six-helix bundle structure and of the individual helical monomers by using CNS 1.0 (*73*). Figures were generated with SETOR (*74*), Insight II (Accelrys), and GRASP (*75*).

RESULTS AND DISCUSSION

Identification of the N57/C42 Complex. To investigate the interaction between the two predicted HR regions in HCoV-NL63 S2 (Figure 1a), we constructed a recombinant protein, denoted N66(L6)C50, in which residues 981−1046 and 1237−1286 are covalently tethered by a short flexible linker sequence. N66(L6)C50 was produced by bacterial expression, purified by reverse-phase HPLC, and refolded by renaturation from GuHCl (see Materials and Methods). Circular dichroism (CD) spectroscopy indicates that N66(L6)C50 forms an extremely stable helical structure that does not unfold on heating to 98 °C in TBS (pH 8.0) (data not shown). On the basis of the mean residue ellipticity at 222 nm at 4 °C and 50 μM protein concentration, we estimate that 90 residues (~75% helix content) are in α-helical conformation. However, sedimentation equilibrium measurements indicate that N66(L6)C50 does not form a monodisperse species and exhibits an apparent molecular mass ranging ~45−180 kDa as a total protein concentration increases from 25 to 400 μM. Hence, the recombinant protein construct associates to form higher-order complexes.

To trim unfolded regions that potentially contribute to the aggregation, N66(L6)C50 was subjected to limited proteolysis by proteinase K. This digestion generates two proteolytic fragments. An N-terminal fragment corresponds to residues 981−1037 (N57), and a C-terminal fragment corresponds to residues 1242−1283 (C42) (Figure 1b). Because proteinase K is not sequence specific, the proteolytic fragments N57 and C42 may more accurately define the α-helical domain structure. Accordingly, we adopted the peptides N57 and C42 for further study. We produced a bacterially expressed single-chain model, designated N57(L10)C42, for the N57/C42 complex. In this construct, the two helical segments are connected via the linker Ser-Gly-Gly-Arg-Gly-Ser-Gly-Arg-Gly-Gly.

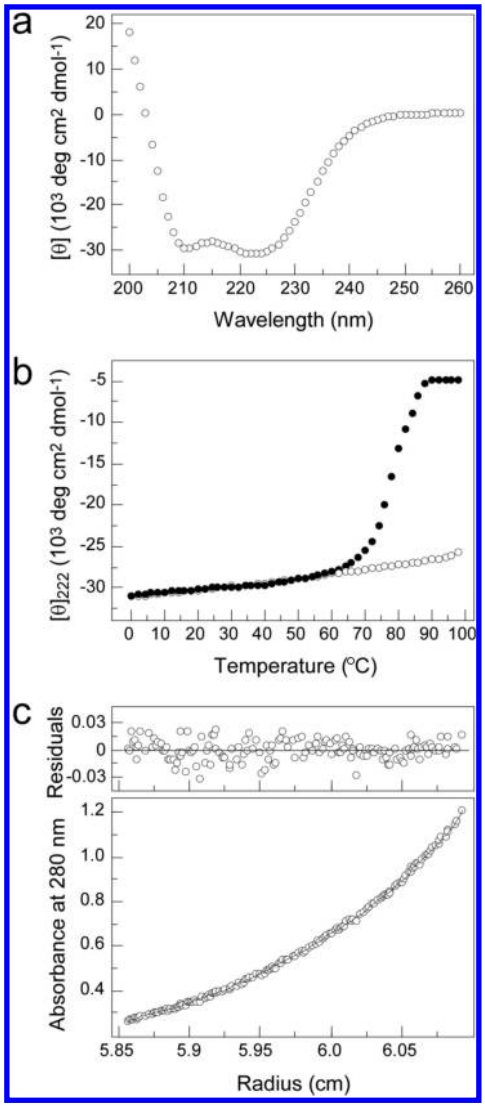

FIGURE 2: Solution properties of N57(L10)C42. (a) Circular dichroism spectrum at 4 °C in TBS (pH 8.0) and 50 μM protein concentration. (b) Thermal melt monitored by CD at 222 nm. The filled circles show data collected in the presence of 5 M GuHCl, a chemical denaturant. (c) Sedimentation equilibrium data for a 100 μM sample at 20 °C and 16 krpm in TBS (pH 8.0). The deviation in the data from the linear fit for a trimeric model is plotted (upper).

Solution Properties of the N57/C42 Complex. The N57-(L10)C42 protein contains >90% helical structure at 4 °C and 50 μM protein concentration in TBS (pH 8.0), as judged by CD studies (Figure 2a). Under these conditions, N57-(L10)C42 has a thermal stability that exceeds 100 °C and unfolds cooperatively and reversibly with a midpoint thermal denaturation (T_m) of 78 °C in the presence of 5 M GuHCl (Figure 2b). Over a 16-fold range of protein concentrations, the observed molecular mass of N57(L10)C42 is 36.9 kDa in TBS (pH 8.0), as determined by sedimentation equilibrium

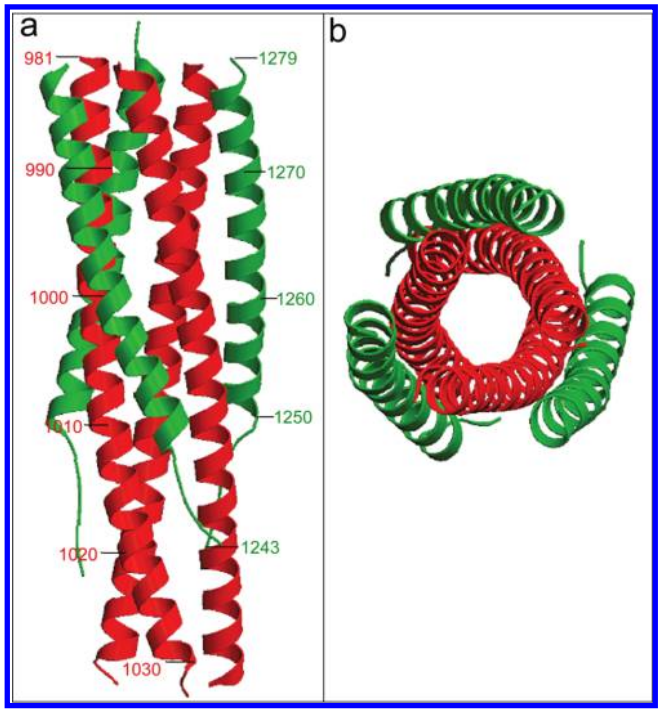

FIGURE 3: Crystal structure of the HCoV-NL63 N57(L10)C42 complex. (a) Lateral view of the N57(L10)C42 trimer. The N57 helices are shown in red and the C42 helices in green. The N termini of the N57 helices point toward the top of the page, and those of the C42 helices point toward the bottom. Residues are numbered according to their position in the HCoV-NL63 S sequence. (b) Axial view of the N57(L10)C42 trimer. The view is from the N termini of the N57 helices looking down the 3-fold axis of the trimer.

experiments (Figure 2c). This value, compared with the expected molecular mass of 35.1 kDa for a trimer, indicates that N57(L10)C42 exists in a discretely trimeric state in solution. Thus, the extra-terminal residues in N66 and C42 trimmed by proteinase K arguably contribute to aggregation of N66(L6)C50. In summary, the slightly smaller N57(L10)-C42 domain forms an exceedingly stable, soluble trimeric-helical structure.

Crystal Structure of N57(L10)C42. The X-ray crystal structure of N57(L10)C42 was determined at 1.75 Å resolution by molecular replacement using the six-helix structure of the SARS-CoV N50/C36 complex as a search model (see Materials and Methods). The final experimental electron density map is of good quality and reveals the positions of all of the amino acid residues except for a few disordered ones at the chain termini and in the interhelical linker. The refined model has an *R*-factor of 19.6% and a free *R*-value of 24.0%. Data collection and refinement statistics are summarized in Table 1. Despite asymmetric crystal contacts, the three individual chains in the N57(L10)C42 structure have essentially the same conformation and degree of order with the average *B*-factors varying from 21 to 23 Å^2. (Note that the connection of an N57 helix to a C42 helix is disordered and not visible in the current structure.) The three N57 and three C42 helices in the noncrystallographic trimer can be superimposed on each other with a rms deviation for the C_α atoms of 0.2−0.3 Å and with the largest deviations occurring at their ends.

As anticipated, N57(L10)C42 is a six-stranded helical bundle (Figure 3). An approximate 3-fold axis of symmetry coincides with the superhelical axis. Each polypeptide chain has an α-helical hairpin conformation (note that the 10-residue peptide linker region is not visible in the electron density maps and therefore must be disordered). The N57 helices form an interior, parallel trimeric coiled coil. Three C42 helices pack in a left-handed and antiparallel direction into hydrophobic grooves on the surface of this coiled-coil trimer. The six-helix bundle forms an overall rod-shaped structure approximately 78 Å in length with a maximum diameter of 28 Å. The N terminus of N57 and the C terminus of C42 are oriented at the same end of the rod-shaped structure (Figure 3a). The N-terminal end of C42 is ∼14 Å from the C-terminal end of the N57 trimer. This packing arrangement would serve to oppose the fusion peptides and transmembranes anchors, and therefore the attached target and viral membranes, into close proximity.

Core Packing in the N57 Parallel Three-Stranded Coiled Coil. The N57 coiled-coil core includes approximately 48 residues (984−1031) from each chain (the most N-terminal residue and the five most C-terminal residues cannot be seen in the electron density maps). Fourteen hydrophobic and three polar residues from each N57 peptide are packed in layers at the coiled-coil interface (Figure 4a). These core amino acids can be grouped into seven heptad repeats (Figure 4f). The last two of these repeats exhibit canonical knobs-into-holes packing, in which the side-chains of the *a* and *d* residues in one α-helix point directly into the hole formed between the side-chains of four residues in an adjacent helix (Figure 4b,c). The angles between the $C_\alpha-C_\alpha$ and $C_\alpha-C_\beta$ vectors at the *a* and *d* layers are 120° and 150°, respectively. This acute packing geometry is characteristic of parallel trimeric coiled coils (*70*, *76*−*78*). In contrast, the first five heptad repeats of N57 lack any regular 3−4 hydrophobic periodicity. Instead, cross-sectional layers containing an "*x*-like" symmetric pattern (Figure 4d) (*79*) alternate with layers containing a *da*-like two-residue pattern (we refer to this as "*y*-like" packing by analogy; see Figure 4e) (*52*). Side chains at the *x* position project simultaneously toward the center of the hydrophobic core (Figure 4d), and similarly alternating small and large side chains at the *y* positions pack in a hexagonal arrangement (Figure 4e). All these core side chains (excluding alanine) adopt their well-populated rotamer conformations in α-helices (*80*).

Because a knobs-into-knobs packing core at the *x* position can cause underwinding and bending of the helix, *y* layers often need to compensate for the existence of *x* layers in the coiled-coil structure (*79*). This type of packing geometry also tends to have small side chains at the first position of the *yy* residues in order to preclude clashes (*81*). The structural result of this *x*−*y*−*y* sequence motif is exactly what we observed in the N57 trimeric coiled coil (Figure 4f): Ile986-Ser989-Phe990, Val993-Ala996-Ile997, Thr1000-Ala1003-Ile1004, and Val1007-Ala1010-Leu1011. In contrast to the C-terminal part of the N57 coiled coil that has a superhelical pitch value of 138 Å, the pitch of the N-terminal *x*−*y*−*y* segment is 214 Å. Increasing the pitch of the supercoil (i.e., underwinding) gives rise to specific non-close-packed layers at the sites of the heptad phase shifts (Figure 4d,e), as compared with close knobs-into-holes side-chain packing seen in the *a* and *d* layers (Figure 4b,c). Although the presence of one or two *x*−*y*−*y* breaks in coiled-coil sequences has been observed in other viral fusion proteins (see Figure 4f) (*52*, *82*, *83*), the combined *x*- and *y*-like

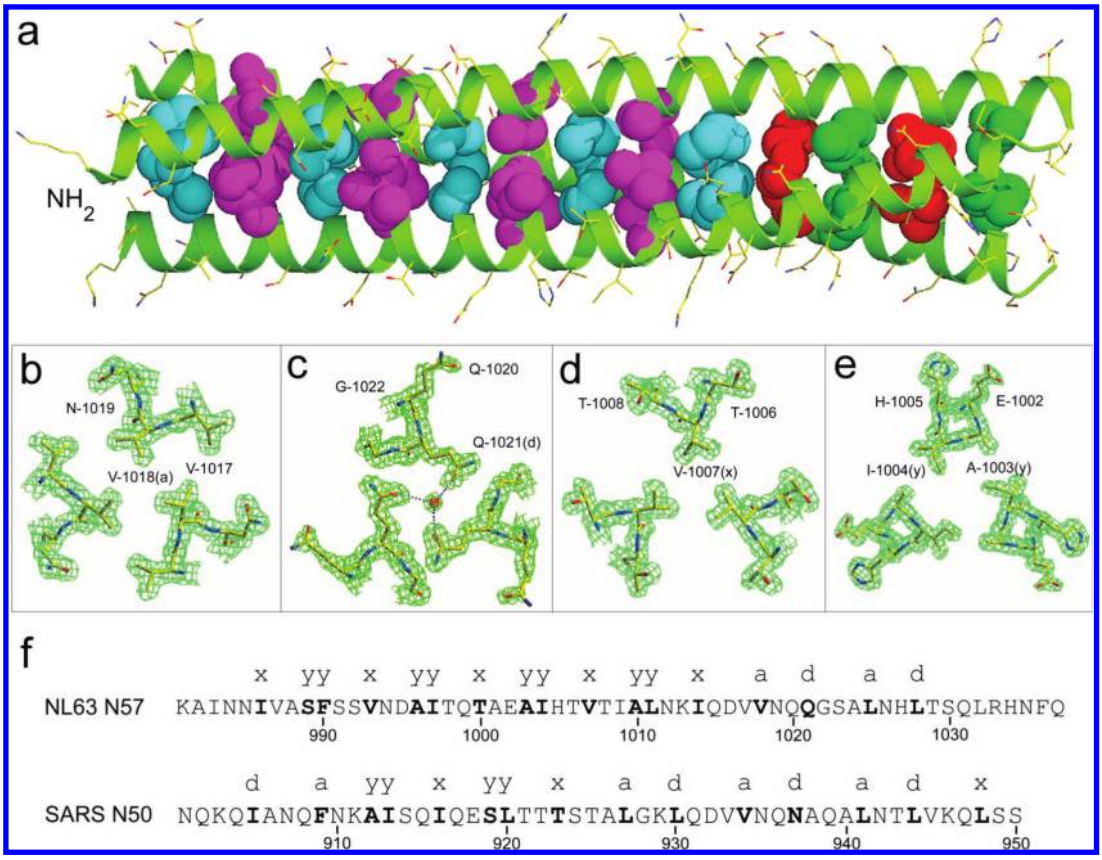

FIGURE 4: Core packing in the N57 parallel coiled-coil trimer. (a) Lateral view of the trimer. Red van der Waals surfaces identify residues at the *a* positions, green surfaces identify residues at the *d* positions, blue surfaces identify residues at the *x* positions, and yellow surfaces identify residues at the *y* positions. (b) Cross-section of the trimer in the Val1018 (*a*) layer. The $2F_o - F_c$ electron density map (contoured at 1.5 σ) is shown with the refined molecular model. (c) Cross-section of the trimer in the Gln1021 (*d*) layer. The glutamine side chains form hydrogen bonds to a bound water molecule (red sphere) in the trimer core at distances ranging 2.61−2.96 Å. Hydrogen bonds are shown as purple dotted lines. (d) The "*x*-like" packing of Val1007 pointing toward the 3-fold symmetry axis. (e) The "*y*-like" packing of Ala1003 and Ile1004 with the alternating small and large side-chains facing inward to form a hydrophobic core. (f) Sequences of the HCoV-NL63 N57 and SARS-CoV N50 (*52*) peptides with the observed heptad-repeat positions. Amino acids at the *a*, *d*, *x*, and *y* positions are in boldface. The residues are numbered according to their position in the HCoV-NL63 and Urbani SARS-CoV S sequences, respectively.

packing geometry spanning the entire nine helical turns has not been seen before.

Interactions between the N57 and C42 Helices. The C-terminal 32 residues of C42 form a nine-turn amphipathic α-helix; amino acids 1244−1247 are in an extended conformation (the two most N-terminal residues and the four most C-terminal residues are disordered). Each C42 chain packs into a hydrophobic groove formed by the interface of adjacent N57 helices, and there are no contacts between individual C42 chains (Figure 5a). Interestingly, the helical region of C42 intercalates into the groove on the outside of the flattened coiled-coil segment (residues 984−1016; Figure 5f). Side chains of the *x* and *y* residues in the coiled-coil core point into the triangular interhelical space between two N57 helices and a buttressing C42 helix (Figure 5b,c). Residues at position *a* of C42 pack against residues at the *x* position of the N57 trimer, and similarly, residues at positions *d* and *e* of C42 fix residues at the *y* positions of N57 (Figure 5f). This interfacial interaction utilizes a "ridges-into-grooves" packing mode found in globular proteins (*84*), in which the ridges are formed by the *a*, *d*, and *e* side chains of C42, and the grooves are lined with the *x* and *y* side chains of N57. Beyond buttressing the N-terminal α-helix, the extended peptide region of C42 fits into the adjoining groove of the N57 coiled coil, forcing the C-terminal end of C42 into a rodlike structure (Figure 5a). The Leu1246 side chain forms van der Waals contacts with the successive layers formed by Ile1014 and Val1018 in the center of the coiled coil.

The interaction of each C42 chain with the N57 trimer buries ∼3164 Å^2 of solvent-accessible surface area. As a result, the net hydrophobic stabilization energy estimated by the method of Eisenberg and McLachlan (*85*) is −43.5 kcal/mol for the interaction. This result supports the view that the driving force for the N57/C42 complex formation is the hydrophobic packing between the outer-layer C42 helices and the interior coiled-coil trimer. Moreover, this interacting surface is interspersed with two polar residues from each N57 chain as well as three polar amino acids and two charged residues from each C42 chain (Figure 5f). These buried polar interactions, in conjunction with nonclassical coiled-coil core packing, appear to be critical in guiding formation of the six-helix bundle. For example, the side chain of Thr1000 at the *x* position of the coiled-coil trimer is oriented so as to allow its hydroxyl group to hydrogen-bond with the carbonyl oxygen of Ala996 (*y*) of the same chain at distances ranging 2.74−2.88 Å, for example (Figure 5d). During the refinement of the structure, 8.6, 6.5, and 4.4 σ peaks of electron density appeared near the N termini of C42 helices A, B, and C, respectively, which were modeled as sodium ions (see Materials and Methods). The side chain of Glu1251 of each C42 helix coordinates to a sodium ion and forms a salt-bridge

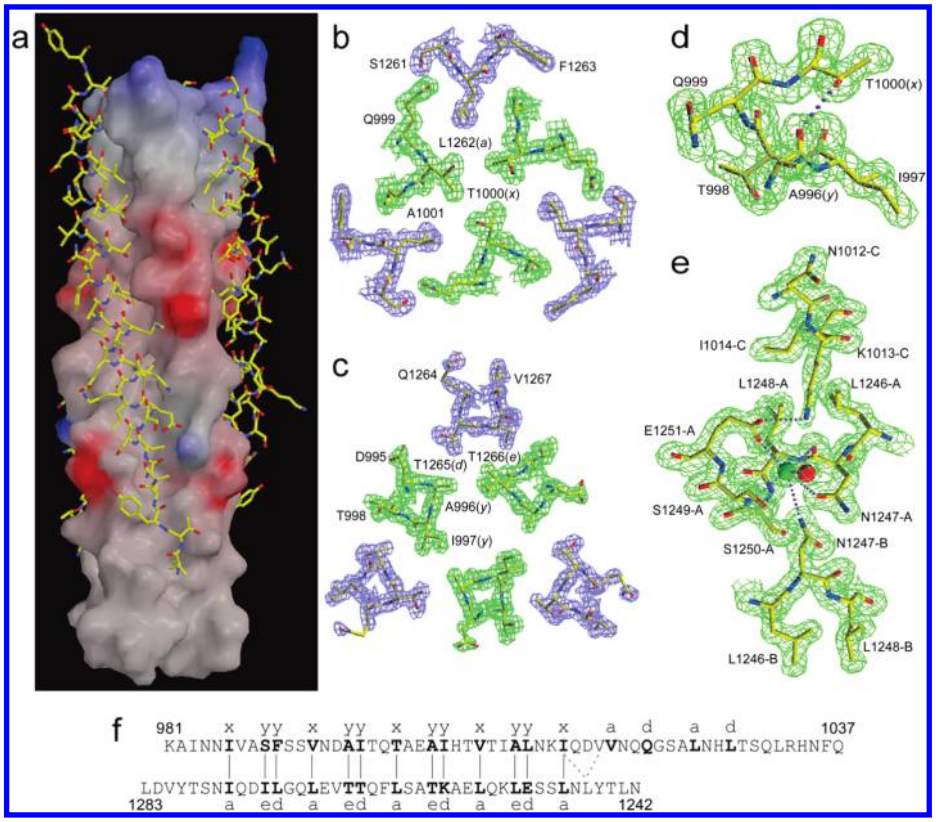

FIGURE 5: Interhelical packing interactions in the N57/C42 complex. (a) Surface properties of the N57 coiled-coil trimer with the C42 chains drawn as an atomic model. The solvent-accessible surface is colored according to the local electrostatic potential, ranging from +12 V in dark blue (most positive) to −19 V in deep red (most negative). (b) Cross-section of the N57(L10)C42 trimer showing that side-chain packing of Leu1262 (blue) at the *a* position of C42 against Thr1000 (green) at the *x* position of N57. The $2F_o - F_c$ electron density map (contoured at 1.5 σ) is shown with the refined molecular model. (c) Cross-section of the N57(L10)C42 trimer showing side-chain packing of Thr1265 and Thr1266 (blue) at the *d* and *e* positions of C42 against Ala996 and Ile997 (green) at the *y* positions of N57. (d) A buried hydrogen-bonding interaction between the side chain of Thr1000 (*x*) and the carbonyl group of Ala996 (*y*). Hydrogen bonds are shown as purple dotted lines. (e) A buried interhelical salt-bridge between Glu1251 (*d*) and Lys1013; the carboxylate group coordinates to a bound sodium ion (pink sphere). (f) Schematic representation of packing interactions between two N57 helices and a C42 helix. Packing interactions between residues at positions *x* and *y* of N57 and residues at positions *a*, *d*, and *e* of C42 are indicated by solid lines. The side chain of Leu1246 of C42 packs against Ile1014 (*x*) and Val1018 (*a*) of N57 (indicated by dotted lines).

with Lys1013 (Oϵ−Nδ = 2.79 Å), and it is packed against Leu1011 at the *y* position of the central coiled-coil trimer (Figure 5e). All of the interfacial residues at the buried core positions of this N57/C42 complex are highly conserved among the group 1 S2 proteins (Figure 1b), presumably reflecting selective pressure on both trimeric coiled-coil interactions and specific interactions between the HR regions in membrane fusion.

Comparison with Other Coronavirus S2 Protein Structures. The N57/C42 complex shows structural similarity to soluble S2 cores from SARS-CoV and MHV (*45*−*48*, *52*), although HCoV-NL63 S2 contains 14-residue in-phase insertions in both HR sequences (Figure 1b). The three six-helix bundles can be superimposed on each other with a root-mean-square (rms) deviation for the C_α atoms of 1.5−4.1 Å and with better superposition of the inner N-peptide coiled-coil core than the outer-layer C peptide (Figure 6). The trimeric coiled coil of MHV S2 has a regular 3−4 hydrophobic periodicity (*48*); the HCoV-NL63 and SARS-CoV coiled coils are atypical because they contain heptad-repeat anomalies, generating the so-called "*x* layers" and "*y* layers". Each of these layers has its own distinguishing geometry, but both display non-close-core packing of apolar residues. As in the HCoV-NL63 S2 core structure, the flattened coiled-coil segment comprising four successive alternating *x* and *y* layers provides a snug fit for intercalation of the C-terminal α-helical region of HR2. In addition, the C-terminal helices pack against a central N-terminal coiled coil with very different conformations in the three soluble S2 core structures.

Biological Implications. The structural and thermodynamic features of the proteolytically resistant S2 core from HCoV-NL63 presented here provide an opportunity to investigate several factors to be considered in the analysis of S glycoprotein-mediated virus entry. First, formation of the stable six-helix bundle in S2 drives the C-terminal transmembrane anchor toward the fusion peptide, allowing the two membrane attachment points to come together in the trimer-of-hairpins structure (*40*−*43*). The N57/C42 structure is a trimer of helical hairpins and likely represents the fusogenic conformation of the HCoV-NL63 S2 protein. Although its overall architecture resembles those of the SARS-CoV and MHV S2 cores, the N57/C42 structure includes significant variations due to the presence of 14-residue insertions in both HR sequences. The six-helix bundle formed by the N57 and C42 peptides shows an extensive *x*−*y*−*y*-like coiled-coil packing interaction. As a consequence, the 32-residue α-helix of each C42 peptide intercalates into the hydrophobic core of the central N-terminal coiled coil. By contrast, the SARS-CoV and MHV S2 cores

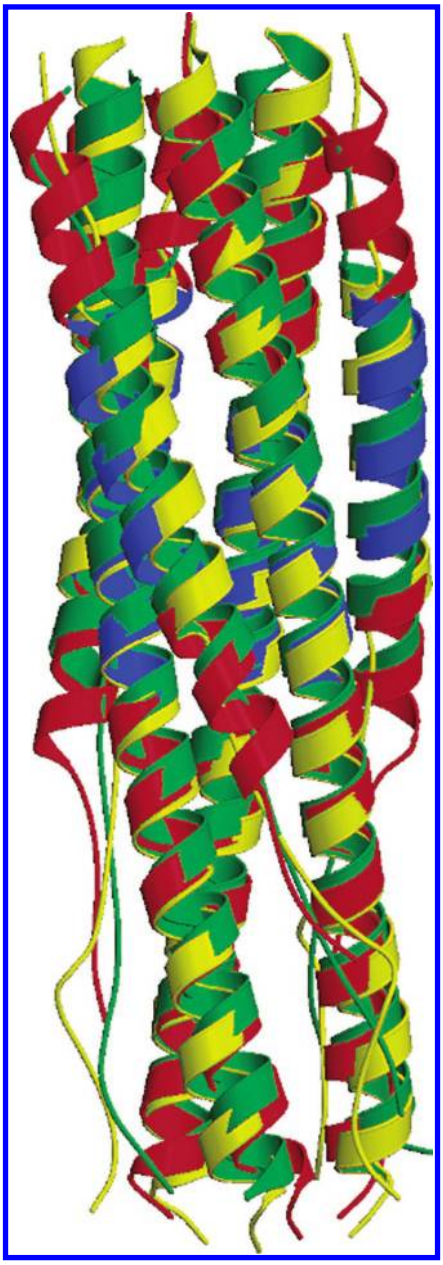

FIGURE 6: Comparison of the N57/C42 complex with the structures of the SARS-CoV and MHV S protein fusion cores. The figure shows superposition of main chain coordinates for the HCoV-NL63 N57/C42 (red), SARS-CoV N50/C36 (1ZV8; green) and MHV 2-Helix (1DWF; yellow) structures. Residues 901−949 and 1152−1182 of SARS-CoV S2 (*52*) and 970−1023 and 1216−1252 of MHV S2 (*48*) are included. The N termini of N helices point toward the top of the page, and those of C helices point toward the bottom. The positions of the 14-residue sequence insertions (blue) in HCoV-NL63 S2 are shown. The largest deviations occur at the N- and C-terminal ends of the C peptide regions in the six-helix bundle structures.

demonstrate more regular core packing geometry, and the numbers of helical residues in their corresponding C-peptides are 19 and 22, respectively (*45*, *46*, *48*, *52*). Thermal unfolding studies show that the N57/C42 complex is exceedingly stable, with a T_m value of 78 °C at 50 μM protein concentration in the presence of the denaturant GuHCl at 5 M concentration. At lower denaturant concentrations, the soluble S2 cores from SARS-CoV and MHV are less stable (*22*, *49*, *52*, *86*). The greater conformational stability of the N57/C42 complex can be ascribed to the large interfacial contacts between the N- and C-peptide helices. This unusually large binding energy may contribute to driving further conformational changes in the group 1 coronaviruses (see below).

Second, we previously suggested that the HR regions, initially sequestered in the native S glycoprotein spike, are released and refold to promote membrane fusion (*52*). C-peptide fusion inhibitors are likely to act during this process by binding to the N-peptide triple-stranded coiled coil in a transient "prehairpin" intermediate, thereby disrupting trimer-of-hairpins formation and blocking viral entry (*40* and references therein). In the coronaviruses, synthetic C-peptides inhibit entry of the HCoV-NL63, MHV, and SARS-CoV viruses with IC_{50} values of 0.5, 0.9, and 17.0 μM, respectively (*50*, *55*, *56*). The high thermodynamic stability of the N57/C42 complex suggests that the exogenous C-peptides could exhibit a high binding affinity for the S2 prehairpin intermediate. We should nonetheless emphasize that the atypical central coiled-coil conformation observed in the N57/C42 structure is likely to be unstable in isolation (see above). This property could therefore result in only transient exposure of the C-peptide binding site on the HCoV-NL63 S2 intermediate state and place temporal restrictions for C-peptide inhibition. Further analysis of the S2 activation process for a kinetic dependence of C-peptide inhibition may aid the development of improved HCoV-NL63 fusion inhibitors.

Third, viral envelope glycoproteins that contain class I fusion moieties are typically synthesized as single-chain precursors and subsequently cleaved by a cellular protease to yield the canonical receptor-binding and transmembrane fusion subunits (*40*−*44*). This maturational cleavage is required for subsequent activation of the membrane fusion activity required for infectivity (*44*, *87*). Interestingly, the S glycoproteins of the group 1 coronaviruses including HCoV-NL63 are not subjected to proteolytic cleavage during biogenesis (*28*−*30*). In contrast, the group 2 viruses such as MHV and the avian group 3 viruses express an S glycoprotein that is cleaved into two noncovalently associated subunits (S1 and S2) by furin-like enzymes during processing in the Golgi in the producer cell (*22*, *24*−*27*). The stabilizing effects of the unique 14-residue insertions on the six-helix bundle structure of the group 1 viruses may offer a mechanistic explanation of this dimorphism in proteolytic maturation of the coronavirus S glycoprotein precursors. We propose that the highly favorable interactions between the extended HR regions of the group 1 viruses constitute a reservoir of free energy in the uncleaved S glycoprotein, primed to drive the S2 fusion reaction when triggered by viral interaction with the target cell. Lack of proteolytic cleavage in the group 1 S glycoproteins might thus be evolutionarily linked to formation of the extremely stable trimer-of-hairpins structure. In this regard, it is noteworthy that the recently emerged SARS-CoV presents an exception to this model in expressing an uncleaved spike that lacks the HR insertion sequences (*29*, *30*, *35*, *39*, *88*). Recent studies suggest that entry by SARS-CoV is dependent on proteolysis of the S glycoprotein by cysteine protease cathepsin L in late endosomal or lysosomal compartment in the target cell (*89*). In contrast, HCoV-NL63 entry, which utilizes the same receptor, is not dependent on cathepsin activity (*90*), although the involvement of another host protease cannot be ruled out at present.

Cleavage of the SARS-CoV S glycoprotein during endocytosis may enable the large-scale structural transitions required for membrane fusion. Thus, it is possible that the group 1 coronaviruses have evolved a different machinery to cooperatively link proteolytic processing and membrane fusion, potentially resulting in additional spatial or temporal regulation. The HCoV-NL63 S2 core structure serves as the starting point for addressing the role of proteolytic maturation in coronavirus membrane fusion and entry.

ACKNOWLEDGMENT

We thank John Schwanof and Randy Abramowitz at the National Synchrotron Light Source for support at beamline X4C, Krzysztof Pyrc for cloning of the human coronavirus NL63 S gene, and a referee for his especially perceptive comments on the manuscript.

REFERENCES

1. Stadler, K., Masignani, V., Eickmann, M., Becker, S., Abrignani, S., Klenk, H. D., and Rappuoli, R. (2003) SARS—beginning to understand a new virus, *Nat. Rev. Microbiol. 1*, 209−218.
2. Peiris, J. S., Yuen, K. Y., Osterhaus, A. D., and Stohr, K. (2003) The severe acute respiratory syndrome, *N. Engl. J. Med. 349*, 2431−2441.
3. Brian, D. A., and Baric, R. S. (2005) Coronavirus genome structure and replication, *Curr. Top. Microbiol. Immunol. 287*, 1−30.
4. McIntosh, K. (2005) Coronaviruses in the limelight, *J. Infect. Dis. 191*, 489−491.
5. van der Hoek, L., Pyrc, K., Jebbink, M. F., Vermeulen-Oost, W., Berkhout, R. J., Wolthers, K. C., Wertheim-van Dillen, P. M., Kaandorp, J., Spaargaren, J., and Berkhout, B. (2004) Identification of a new human coronavirus, *Nat. Med. 10*, 368−373.
6. Fouchier, R. A., Hartwig, N. G., Bestebroer, T. M., Niemeyer, B., de Jong, J. C., Simon, J. H., and Osterhaus, A. D. (2004) A previously undescribed coronavirus associated with respiratory disease in humans, *Proc. Natl. Acad. Sci. U.S.A. 101*, 6212−6216.
7. Esper, F., Weibel, C., Ferguson, D., Landry, M. L., and Kahn, J. S. (2005) Evidence of a novel human coronavirus that is associated with respiratory tract disease in infants and young children, *J. Infect. Dis. 191*, 492−498.
8. van der Hoek, L., Sure, K., Ihorst, G., Stang, A., Pyrc, K., Jebbink, M. F., Petersen, G., Forster, J., Berkhout, B., and Uberla, K. (2005) Croup is associated with the novel coronavirus NL63, *PLoS Med. 2*, e240.
9. Gonzalez, J. M., Gomez-Puertas, P., Cavanagh, D., Gorbalenya, A. E., and Enjuanes, L. (2003) A comparative sequence analysis to revise the current taxonomy of the family Coronaviridae, *Arch. Virol. 148*, 2207−2235.
10. Gibbs, A. J., Gibbs, M. J., and Armstrong, J. S. (2004) The phylogeny of SARS coronavirus, *Arch. Virol. 149*, 621−624.
11. Gorbalenya, A. E., Snijder, E. J., and Spaan, W. J. (2004) Severe acute respiratory syndrome coronavirus phylogeny: toward consensus, *J. Virol. 78*, 7863−7866.
12. Snijder, E. J., Bredenbeek, P. J., Dobbe, J. C., Thiel, V., Ziebuhr, J., Poon, L. L., Guan, Y., Rozanov, M., Spaan, W. J., and Gorbalenya, A. E. (2003) Unique and conserved features of genome and proteome of SARS-coronavirus, an early split-off from the coronavirus group 2 lineage, *J. Mol. Biol. 331*, 991−1004.
13. Kuo, L., Godeke, G. J., Raamsman, M. J., Masters, P. S., and Rottier, P. J. (2000) Retargeting of coronavirus by substitution of the spike glycoprotein ectodomain: crossing the host cell species barrier, *J. Virol. 74*, 1393−1406.
14. Phillips, J. J., Chua, M. M., Lavi, E., and Weiss, S. R. (1999) Pathogenesis of chimeric MHV4/MHV-A59 recombinant viruses: the murine coronavirus spike protein is a major determinant of neurovirulence, *J. Virol. 73*, 7752−7760.
15. Sanchez, C. M., Izeta, A., Sanchez-Morgado, J. M., Alonso, S., Sola, I., Balasch, M., Plana-Duran, J., and Enjuanes, L. (1999) Targeted recombination demonstrates that the spike gene of transmissible gastroenteritis coronavirus is a determinant of its enteric tropism and virulence, *J. Virol. 73*, 7607−7618.
16. Casais, R., Dove, B., Cavanagh, D., and Britton, P. (2003) Recombinant avian infectious bronchitis virus expressing a heterologous spike gene demonstrates that the spike protein is a determinant of cell tropism, *J. Virol. 77*, 9084−9089.
17. Haijema, B. J., Volders, H., and Rottier, P. J. (2003) Switching species tropism: an effective way to manipulate the feline coronavirus genome, *J. Virol. 77*, 4528−4538.
18. Schickli, J. H., Thackray, L. B., Sawicki, S. G., and Holmes, K. V. (2004) The N-terminal region of the murine coronavirus spike glycoprotein is associated with the extended host range of viruses from persistently infected murine cells, *J. Virol. 78*, 9073−9083.
19. Li, W., Wong, S. K., Li, F., Kuhn, J. H., Huang, I. C., Choe, H., and Farzan, M. (2006) Animal origins of the severe acute respiratory syndrome coronavirus: insight from ACE2-S-protein interactions, *J. Virol. 80*, 4211−4219.
20. Lai, M. M. C., and Holmes, K. V. (2001) in *Fields Virology* (Knipe, D. M., and Howley, P. M., Eds.) pp 1163−1185, Lippincott Williams & Wilkins, Philadelphia, PA.
21. Gallagher, T. M., and Buchmeier, M. J. (2001) Coronavirus spike proteins in viral entry and pathogenesis, *Virology 279*, 371−374.
22. Bosch, B. J., van der Zee, R., de Haan, C. A., and Rottier, P. J. (2003) The coronavirus spike protein is a class I virus fusion protein: structural and functional characterization of the fusion core complex, *J. Virol. 77*, 8801−8811.
23. Dimitrov, D. S. (2004) Virus entry: molecular mechanisms and biomedical applications, *Nat. Rev. Microbiol. 2*, 109−122.
24. Frana, M. F., Behnke, J. N., Sturman, L. S., and Holmes, K. V. (1985) Proteolytic cleavage of the E2 glycoprotein of murine coronavirus: host-dependent differences in proteolytic cleavage and cell fusion, *J. Virol. 56*, 912−920.
25. Sturman, L. S., Ricard, C. S., and Holmes, K. V. (1985) Proteolytic cleavage of the E2 glycoprotein of murine coronavirus: activation of cell-fusing activity of virions by trypsin and separation of two different 90K cleavage fragments, *J. Virol. 56*, 904−911.
26. Jackwood, M. W., Hilt, D. A., Callison, S. A., Lee, C. W., Plaza, H., and Wade, E. (2001) Spike glycoprotein cleavage recognition site analysis of infectious bronchitis virus, *Avian Dis. 45*, 366−372.
27. de Haan, C. A., Stadler, K., Godeke, G. J., Bosch, B. J., and Rottier, P. J. (2004) Cleavage inhibition of the murine coronavirus spike protein by a furin-like enzyme affects cell-cell but not virus-cell fusion, *J. Virol. 78*, 6048−6054.
28. Arpin, N., and Talbot, P. J. (1990) Molecular characterization of the 229E strain of human coronavirus, *Adv. Exp. Med. Biol. 276*, 73−80.
29. Moore, M. J., Dorfman, T., Li, W., Wong, S. K., Li, Y., Kuhn, J. H., Coderre, J., Vasilieva, N., Han, Z., Greenough, T. C., Farzan, M., and Choe, H. (2004) Retroviruses pseudotyped with the severe acute respiratory syndrome coronavirus spike protein efficiently infect cells expressing angiotensin-converting enzyme 2, *J. Virol. 78*, 10628−10635.
30. Xiao, X., Chakraborti, S., Dimitrov, A. S., Gramatikoff, K., and Dimitrov, D. S. (2003) The SARS-CoV S glycoprotein: expression and functional characterization, *Biochem. Biophys. Res. Commun. 312*, 1159−1164.
31. Hofmann, H., Pyrc, K., van der Hoek, L., Geier, M., Berkhout, B., and Pohlmann, S. (2005) Human coronavirus NL63 employs the severe acute respiratory syndrome coronavirus receptor for cellular entry, *Proc. Natl. Acad. Sci. U.S.A. 102*, 7988−7993.
32. Li, W., Moore, M. J., Vasilieva, N., Sui, J., Wong, S. K., Berne, M. A., Somasundaran, M., Sullivan, J. L., Luzuriaga, K., Greenough, T. C., Choe, H., and Farzan, M. (2003) Angiotensin-converting enzyme 2 is a functional receptor for the SARS coronavirus, *Nature 426*, 450−454.
33. Yeager, C. L., Ashmun, R. A., Williams, R. K., Cardellichio, C. B., Shapiro, L. H., Look, A. T., and Holmes, K. V. (1992) Human aminopeptidase N is a receptor for human coronavirus 229E, *Nature 357*, 420−422.
34. Delmas, B., Gelfi, J., L'Haridon, R., Vogel, L. K., Sjostrom, H., Noren, O., and Laude, H. (1992) Aminopeptidase N is a major receptor for the entero-pathogenic coronavirus TGEV, *Nature 357*, 417−420.
35. Simmons, G., Reeves, J. D., Rennekamp, A. J., Amberg, S. M., Piefer, A. J., and Bates, P. (2004) Characterization of severe acute respiratory syndrome-associated coronavirus (SARS-CoV) spike glycoprotein-mediated viral entry, *Proc. Natl. Acad. Sci. U.S.A. 101*, 4240−4245.
36. Yang, Z. Y., Huang, Y., Ganesh, L., Leung, K., Kong, W. P., Schwartz, O., Subbarao, K., and Nabel, G. J. (2004) pH-dependent

entry of severe acute respiratory syndrome coronavirus is mediated by the spike glycoprotein and enhanced by dendritic cell transfer through DC-SIGN, *J. Virol. 78*, 5642−5650.
37. Hofmann, H., Hattermann, K., Marzi, A., Gramberg, T., Geier, M., Krumbiegel, M., Kuate, S., Uberla, K., Niedrig, M., and Pohlmann, S. (2004) S protein of severe acute respiratory syndrome-associated coronavirus mediates entry into hepatoma cell lines and is targeted by neutralizing antibodies in infected patients, *J. Virol. 78*, 6134−6142.
38. Gallagher, T. M., Escarmis, C., and Buchmeier, M. J. (1991) Alteration of the pH dependence of coronavirus-induced cell fusion: effect of mutations in the spike glycoprotein, *J. Virol. 65*, 1916−1928.
39. Follis, K. E., York, J., and Nunberg, J. H. (2006) Furin cleavage of the SARS coronavirus spike glycoprotein enhances cell-cell fusion but does not affect virion entry, *Virology 350*, 358−369.
40. Eckert, D. M., and Kim, P. S. (2001) Mechanisms of viral membrane fusion and its inhibition, *Annu. Rev. Biochem. 70*, 777−810.
41. Earp, L. J., Delos, S. E., Park, H. E., and White, J. M. (2005) The many mechanisms of viral membrane fusion proteins, *Curr. Top. Microbiol. Immunol. 285*, 25−66.
42. Weissenhorn, W., Dessen, A., Calder, L. J., Harrison, S. C., Skehel, J. J., and Wiley, D. C. (1999) Structural basis for membrane fusion by enveloped viruses, *Mol. Membr. Biol. 16*, 3−9.
43. Harrison, S. C. (2005) Mechanism of membrane fusion by viral envelope proteins, *Adv. Virus Res. 64*, 231−261.
44. Skehel, J. J., and Wiley, D. C. (2000) Receptor binding and membrane fusion in virus entry: the influenza hemagglutinin, *Annu. Rev. Biochem. 69*, 531−569.
45. Xu, Y., Lou, Z., Liu, Y., Pang, H., Tien, P., Gao, G. F., and Rao, Z. (2004) Crystal structure of severe acute respiratory syndrome coronavirus spike protein fusion core, *J. Biol. Chem. 279*, 49414−49419.
46. Supekar, V. M., Bruckmann, C., Ingallinella, P., Bianchi, E., Pessi, A., and Carfi, A. (2004) Structure of a proteolytically resistant core from the severe acute respiratory syndrome coronavirus S2 fusion protein, *Proc. Natl. Acad. Sci. U.S.A. 101*, 17958−17963.
47. Duquerroy, S., Vigouroux, A., Rottier, P. J., Rey, F. A., and Bosch, B. J. (2005) Central ions and lateral asparagine/glutamine zippers stabilize the post-fusion hairpin conformation of the SARS coronavirus spike glycoprotein, *Virology 335*, 276−285.
48. Xu, Y., Liu, Y., Lou, Z., Qin, L., Li, X., Bai, Z., Pang, H., Tien, P., Gao, G. F., and Rao, Z. (2004) Structural basis for coronavirus-mediated membrane fusion. Crystal structure of mouse hepatitis virus spike protein fusion core, *J. Biol. Chem. 279*, 30514−30522.
49. Ingallinella, P., Bianchi, E., Finotto, M., Cantoni, G., Eckert, D. M., Supekar, V. M., Bruckmann, C., Carfi, A., and Pessi, A. (2004) Structural characterization of the fusion-active complex of severe acute respiratory syndrome (SARS) coronavirus, *Proc. Natl. Acad. Sci. U.S.A. 101*, 8709−8714.
50. Liu, S., Xiao, G., Chen, Y., He, Y., Niu, J., Escalante, C. R., Xiong, H., Farmar, J., Debnath, A. K., Tien, P., and Jiang, S. (2004) Interaction between heptad repeat 1 and 2 regions in spike protein of SARS-associated coronavirus: implications for virus fusogenic mechanism and identification of fusion inhibitors, *Lancet 363*, 938−947.
51. Tripet, B., Howard, M. W., Jobling, M., Holmes, R. K., Holmes, K. V., and Hodges, R. S. (2004) Structural characterization of the SARS-coronavirus spike S fusion protein core, *J. Biol. Chem. 279*, 20836−20849.
52. Deng, Y., Liu, J., Zheng, Q., Yong, W., and Lu, M. (2006) Structures and polymorphic interactions of two heptad-repeat regions of the SARS virus S2 protein, *Structure 14*, 889−899.
53. Russell, C. J., Jardetzky, T. S., and Lamb, R. A. (2001) Membrane fusion machines of paramyxoviruses: capture of intermediates of fusion, *Embo J. 20*, 4024−4034.
54. Melikyan, G. B., Markosyan, R. M., Hemmati, H., Delmedico, M. K., Lambert, D. M., and Cohen, F. S. (2000) Evidence that the transition of HIV-1 gp41 into a six-helix bundle, not the bundle configuration, induces membrane fusion, *J. Cell Biol. 151*, 413−423.
55. Bosch, B. J., Martina, B. E., Van Der Zee, R., Lepault, J., Haijema, B. J., Versluis, C., Heck, A. J., De Groot, R., Osterhaus, A. D., and Rottier, P. J. (2004) Severe acute respiratory syndrome coronavirus (SARS-CoV) infection inhibition using spike protein heptad repeat-derived peptides, *Proc. Natl. Acad. Sci. U.S.A. 101*, 8455−8460.
56. Pyrc, K., Bosch, B. J., Berkhout, B., Jebbink, M. F., Dijkman, R., Rottier, P., and van der Hoek, L. (2006) Inhibition of human coronavirus NL63 infection at early stages of the replication cycle, *Antimicrob. Agents Chemother. 50*, 2000−2008.
57. Kleid, D. G., Yansura, D., Small, B., Dowbenko, D., Moore, D. M., Grubman, M. J., McKercher, P. D., Morgan, D. O., Robertson, B. H., and Bachrach, H. L. (1981) Cloned viral protein vaccine for foot-and-mouth disease: responses in cattle and swine, *Science 214*, 1125−1129.
58. Shu, W., Ji, H., and Lu, M. (1999) Trimerization specificity in HIV-1 gp41: analysis with a GCN4 leucine zipper model, *Biochemistry 38*, 5378−5385.
59. Edelhoch, H. (1967) Spectroscopic determination of tryptophan and tyrosine in proteins, *Biochemistry 6*, 1948−1954.
60. Chen, Y. H., Yang, J. T., and Chau, K. H. (1974) Determination of the helix and beta form of proteins in aqueous solution by circular dichroism, *Biochemistry 13*, 3350−3359.
61. Cantor, C., and Schimmel, P. (1980) *Biophys. Chem.*, Vol. 3, W. H. Freeman and Co., New York.
62. Johnson, M. L., Correia, J. J., Yphantis, D. A., and Halvorson, H. R. (1981) Analysis of data from the analytical ultracentrifuge by nonlinear least-squares techniques, *Biophys. J. 36*, 575−588.
63. Laue, T. M., Shah, B. D., Ridgeway, T. M., and Pelletier, S. L. (1992) in *Analytical Ultracentrifugation in Biochemistry and Polymer Science* (Horton, J. C., Ed.) pp 90−125, Royal Society of Chemistry, Cambridge, U.K.
64. Otwinowski, Z., and Minor, W. (1997) Processing X-ray diffraction data collected in oscillation mode, *Methods Enzymol. 276*, 307−326.
65. Storoni, L. C., McCoy, A. J., and Read, R. J. (2004) Likelihood-enhanced fast rotation functions, *Acta Crystallogr. D Biol. Crystallogr. 60*, 432−438.
66. Lamzin, V. S., and Wilson, K. S. (1993) Automated refinement of protein models, *Acta Crystallogr. D 49*, 129−149.
67. Jones, T. A., Zou, J. Y., Cowan, S. W., and Kjeldgaard, M. (1991) Improved methods for building protein models in electron density maps and the location of errors in these models, *Acta Crystallogr. A 47*, 110−119.
68. Murshudov, G. N., Vagin, A. A., and Dodson, E. J. (1997) Refinement of macromolecular structures by the maximum-likehood method, *Acta Crystallogr. D 53*, 240−255.
69. Schomaker, V., and Trueblood, K. N. (1998) Correlation of internal torsional motion with overall molecular motion in crystals, *Acta Crystallogr. B 54*, 507−514.
70. Crick, F. H. C. (1953) The packing of α-helices: simple coiled-coils, *Acta Crystallogr. 6*, 689−697.
71. Strelkov, S. V., and Burkhard, P. (2002) Analysis of alpha-helical coiled coils with the program TWISTER reveals a structural mechanism for stutter compensation, *J. Struct. Biol. 137*, 54−64.
72. Potterton, E., Briggs, P., Turkenburg, M., and Dodson, E. (2003) A graphical user interface to the CCP4 program suite, *Acta Crystallogr. D Biol. Crystallogr. 59*, 1131−1137.
73. Brunger, A. T., Adams, P. D., Clore, G. M., DeLano, W. L., Gros, P., Grosse-Kunstleve, R. W., Jiang, J. S., Kuszewski, J., Nilges, M., Pannu, N. S., Read, R. J., Rice, L. M., Simonson, T., and Warren, G. L. (1998) Crystallography & NMR system: A new software suite for macromolecular structure determination, *Acta Crystallogr. D Biol. Crystallogr. 54* (Pt 5), 905−921.
74. Evans, S. V. (1993) SETOR: hardware-lighted three-dimensional solid model representations of macromolecules, *J. Mol. Graph. 11*, 134−138.
75. Nicholls, A., Sharp, K. A., and Honig, B. (1991) Protein folding and association: insights from the interfacial and thermodynamic properties of hydrocarbons, *Proteins 11*, 281−296.
76. Harbury, P. B., Kim, P. S., and Alber, T. (1994) Crystal structure of an isoleucine-zipper trimer, *Nature 371*, 80−83.
77. Harbury, P. B., Zhang, T., Kim, P. S., and Alber, T. (1993) A switch between two-, three-, and four-stranded coiled coils in GCN4 leucine zipper mutants, *Science 262*, 1401−1407.
78. Liu, J., Yong, W., Deng, Y., Kallenbach, N. R., and Lu, M. (2004) Atomic structure of a tryptophan-zipper pentamer, *Proc. Natl. Acad. Sci. U.S.A. 101*, 16156−16161.
79. Lupas, A. N., and Gruber, M. (2005) The structure of alpha-helical coiled coils, *Adv. Protein Chem. 70*, 37−78.
80. Lovell, S. C., Word, J. M., Richardson, J. S., and Richardson, D. C. (2000) The penultimate rotamer library, *Proteins 40*, 389−408.

81. Brown, J. H., Cohen, C., and Parry, D. A. (1996) Heptad breaks in alpha-helical coiled coils: stutters and stammers, *Proteins 26*, 134−145.
82. Baker, K. A., Dutch, R. E., Lamb, R. A., and Jardetzky, T. S. (1999) Structural basis for paramyxovirus-mediated membrane fusion, *Mol. Cell 3*, 309−319.
83. Weissenhorn, W., Carfi, A., Lee, K. H., Skehel, J. J., and Wiley, D. C. (1998) Crystal structure of the Ebola virus membrane fusion subunit, GP2, from the envelope glycoprotein ectodomain, *Mol. Cell 2*, 605−616.
84. Chothia, C., Levitt, M., and Richardson, D. (1981) Helix to helix packing in proteins, *J. Mol. Biol. 145*, 215−250.
85. Eisenberg, D., and McLachlan, A. D. (1986) Solvation energy in protein folding and binding, *Nature 319*, 199−203.
86. Xu, Y., Cole, D. K., Lou, Z., Liu, Y., Qin, L., Li, X., Bai, Z., Yuan, F., Rao, Z., and Gao, G. F. (2004) Construct design, biophysical, and biochemical characterization of the fusion core from mouse hepatitis virus (a coronavirus) spike protein, *Protein Expression Purif. 38*, 116−122.
87. Scheid, A., and Choppin, P. W. (1974) The hemagglutinating and neuraminidase protein of a paramyxovirus: interaction with neuraminic acid in affinity chromatography, *Virology 62*, 125−133.
88. Song, H. C., Seo, M. Y., Stadler, K., Yoo, B. J., Choo, Q. L., Coates, S. R., Uematsu, Y., Harada, T., Greer, C. E., Polo, J. M., Pileri, P., Eickmann, M., Rappuoli, R., Abrignani, S., Houghton, M., and Han, J. H. (2004) Synthesis and characterization of a native, oligomeric form of recombinant severe acute respiratory syndrome coronavirus spike glycoprotein, *J. Virol. 78*, 10328−10335.
89. Simmons, G., Gosalia, D. N., Rennekamp, A. J., Reeves, J. D., Diamond, S. L., and Bates, P. (2005) Inhibitors of cathepsin L prevent severe acute respiratory syndrome coronavirus entry, *Proc. Natl. Acad. Sci. U.S.A. 102*, 11876−11881.
90. Huang, I. C., Bosch, B. J., Li, F., Li, W., Lee, K. H., Ghiran, S., Vasilieva, N., Dermody, T. S., Harrison, S. C., Dormitzer, P. R., Farzan, M., Rottier, P. J., and Choe, H. (2006) SARS coronavirus, but not human coronavirus NL63, utilizes cathepsin L to infect ACE2-expressing cells, *J. Biol. Chem. 281*, 3198−3203.

BI061686W